



Influence of rotating wheels on Reynolds number sensitivity of passenger vehicle drag

Downloaded from: <https://research.chalmers.se>, 2024-11-06 00:21 UTC





Citation for the original published paper (version of record):

Josefsson, E., Urquhart, M., Sebben, S. (2024). Influence of rotating wheels on Reynolds number sensitivity of passenger vehicle drag. *Physics of Fluids*, 36(9). <http://dx.doi.org/10.1063/5.0226694>

N.B. When citing this work, cite the original published paper.

RESEARCH ARTICLE | SEPTEMBER 30 2024

Influence of rotating wheels on Reynolds number sensitivity of passenger vehicle drag ^{EP}

Erik Josefsson  ; Magnus Urquhart  ; Simone Sebben  



Physics of Fluids 36, 095182 (2024)

<https://doi.org/10.1063/5.0226694>



Articles You May Be Interested In

Floor motion's influence on wake asymmetry of a notchback bluff body

Physics of Fluids (March 2022)

Comparison of flow characteristics behind squareback bluff-bodies with and without wheels

Physics of Fluids (March 2023)

Influence of the rounded rear edge on wake bi-stability of a notchback bluff body

Physics of Fluids (November 2021)



Physics of Fluids

Special Topics Open
for Submissions

[Learn More](#)

Influence of rotating wheels on Reynolds number sensitivity of passenger vehicle drag

Cite as: Phys. Fluids **36**, 095182 (2024); doi: [10.1063/5.0226694](https://doi.org/10.1063/5.0226694)

Submitted: 3 July 2024 · Accepted: 2 September 2024 ·

Published Online: 30 September 2024





View Online



Export Citation



CrossMark

Erik Josefsson,¹  Magnus Urquhart,²  and Simone Sebben^{1,a)} 

AFFILIATIONS

¹Department of Mechanics and Maritime Sciences, Chalmers University of Technology, Gothenburg, Sweden

²Aerodynamics, Volvo Cars, Gothenburg, Sweden

^{a)} Author to whom correspondence should be addressed: simone.sebben@chalmers.se

ABSTRACT

Rotating wheels are essential to replicate realistic forces and flow fields during aerodynamic testing of passenger vehicles. Previous studies have found that the drag coefficient typically reduces with increased speed under rotating wheel conditions but is stable with stationary wheels. This paper investigates this velocity sensitivity for two vehicles, the aerodynamic research vehicle DrivAer and a production vehicle. Experiments with the DrivAer indicate that the drag reduction with increased speed cannot be explained by pressure changes on the vehicle body; instead, the effect is attributed to local flow changes around the wheels. Using numerical simulations, it is found that the separation at the front wheels' outer tire shoulder increases for lower velocities, thus resulting in higher drag coefficient and causing Reynolds number sensitivity. The degree of drag reduction is less for the DrivAer squareback than for the notchback due to the separation over the notchback's rear window. No direct difference is measured between various tires and rims. To assess the generality of the findings with the DrivAer, the results are compared to experiments with a production vehicle. It is observed that the drag sensitivity is less and only occurs if the rear wheels are rotating. Pressure measurements in the wheelhouses and around the wheel drive units confirm the front wheel separation's dependence on velocity and highlight the complex interaction between the front wheel wakes and rear wheel rotational state.

© 2024 Author(s). All article content, except where otherwise noted, is licensed under a Creative Commons Attribution (CC BY) license (<https://creativecommons.org/licenses/by/4.0/>). <https://doi.org/10.1063/5.0226694>

I. INTRODUCTION

Emission legislation and customer expectations of increased electric range create a need for improving the energy efficiency of road vehicles. Aerodynamic drag is one of the largest resistive forces acting on a vehicle, especially at speeds above approximately 70 km/h.¹ It has been shown that the wheels of a passenger vehicle contribute to approximately 25% of the total drag.^{2,3} Therefore, it is important to understand and correctly predict the flow around them.

Many studies have shown that simulating rotating wheels is essential for obtaining realistic flow conditions and that wheel rotation typically reduces drag compared to the stationary case.^{3–8} Eloffsson and Bannister⁵ compared rotating and stationary wheels, concluding that the drag reduction was mainly caused by rotation of the rear wheels. Rear wheel rotation altered the interaction between wheel and base wakes, increasing the base pressure. It was shown that the drag reduction was dependent on the vehicle body, with a sedan experiencing a larger decrease than a squareback. This was explained by an improved wake balance with rotating rear wheels for the sedan. Similar interactions were also established by Wang *et al.*⁸ using a simplified scale

model where wheel rotation, mainly on the rear axle, was found to alter the wake balance and global forces.

While performing velocity sweeps with full-scale vehicles, many studies have found that the drag coefficient, C_D , typically reduces with increased wind speed when the wheels are rotating.^{9–15} With stationary wheels, C_D is typically more stable.^{10,13,14} In 2010, the European Aerodynamic Data Exchange Committee (EADE) performed measurements on eleven vehicles in ten European wind tunnels. The data are not publicly available, but a subset was published by Wolf.¹⁴ From this, it is clear that the drag reduction with speed is a general effect present for multiple vehicles and wind tunnels when testing with rotating wheels.

Wolf¹⁴ tested an SUV coupe with moving ground (rotating wheels and center belt enabled) and found a drag decrease of $0.011 C_D/100$ km/h. Without moving ground, the drag coefficient was almost constant in the range from 60 to 300 km/h. Comparing measurements with only the front or the rear wheels rotating, it was found that the drag-reducing effect was due to rear wheel rotation. However, the state of the front wheels altered the gradient of drag reduction,

showing that there are interference effects between the wheels. It was theorized that the drag reduction was due to an increase in base pressure, similar to the effect described by Elofsson and Bannister⁵ when comparing rotating and stationary wheels. The higher pressure was believed to be caused by larger energy input from the rear wheels with higher rotational speed. Part of the additional energy was believed to come from the ventilation moment needed to rotate the wheels in the airflow. Measuring three wheelsets with 20, 21, and 22 inch rims, it was found that the velocity gradient of C_D was altered, with the largest drag reduction being measured for the largest rim.

Other studies have suggested that the drag reduction is due to tire deformation and how it changes with speed. Landström *et al.*¹¹ described how the tire expands radially and contracts axially with increasing rotational velocity. If the vertical position of the vehicle is fixed in the wind tunnel, the radial expansion will compress the suspension spring, lifting the wheel into the wheelhouse. This results in a narrower tire that occupies more of the wheelhouse volume. Both effects are expected to reduce the drag. Wittmeier¹⁶ showed that a narrower tire typically has lower drag and, based on the results of Cogotti,² it is expected that the drag is reduced when the tire occupies more of the wheelhouse volume. If the vehicle is allowed to move vertically, as is the case during real driving, the wheel deformation and aerodynamic lift on the vehicle body will instead lift the entire vehicle. This has been shown to reduce the gradient of C_D with respect to velocity,¹² which is expected since drag typically increases with ground clearance.¹

The theory that the drag reduction is caused by the deforming tire geometry was strengthened by Reiß¹⁵ who presented velocity sweeps with regular, deformable, tires and rigid alloy wheels from tests with a full-scale DrivAer squareback. The regular tires experienced a reduction of $0.006 C_D/100 \text{ km/h}$ whereas C_D was almost constant with rigid wheels. Considering the simplified case of an isolated wheel, Leśniewicz *et al.*¹⁷ performed RANS simulations and found that the drag reduced with speed. The drag decrease was achieved despite maintaining a constant tire geometry for all velocities, indicating that tire deformation might not be the sole explanation.

Cogotti² presented the Reynolds number dependency of an isolated stationary wheel, Fig. 1. Using the wheel diameter as the length

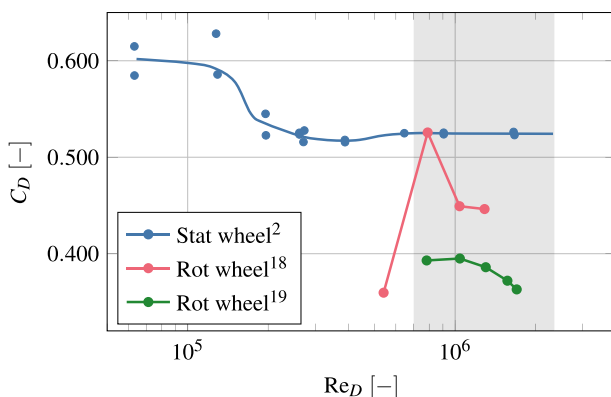


FIG. 1. Drag coefficient as a function of Reynolds number (based on wheel diameter) for stationary and rotating isolated wheels. The wheel geometries are different in the studies. For Ref. 2, a trend line has been fitted to the measured data. The gray area corresponds to the range from 60 to 200 km/h for a full-scale wheel in air.

scale, there is a transition region between 10^5 and 10^6 . The sensitive range overlaps with the aerodynamically relevant region (marked gray in the figure), with 10^6 corresponding to approximately 80 km/h for a full-scale wheel in air. To the best of the authors' knowledge, a similar study over a large range of Reynolds numbers has not been published for a rotating wheel. However, data from both Morelli¹⁸ and Semeraro¹⁹ showed that the drag of a single rotating wheel is sensitive to the Reynolds number, Fig. 1.

From the available literature, it is evident that there is no clear explanation for the drag's Reynolds number sensitivity when testing with rotating wheels. This paper aims to increase this knowledge by studying full-scale vehicles at different velocities. Initially, experiments and simulations with the DrivAer are considered. The flow mechanisms are analyzed for a baseline configuration and the effect of geometrical configurations on the gradient of C_D is studied. Finally, the results are compared to experiments with a production vehicle and the differences are highlighted and discussed.

II. METHODOLOGY

A. Vehicle geometry

1. DrivAer

The DrivAer reference model introduced by Heft *et al.*²⁰ was investigated in the version presented by James *et al.*¹³ It featured a detailed underbody, an engine bay, and a simplified, rigid, suspension system with rotating brake disks. The tests were performed with rear-view mirrors, sealed grilles, and a small airdam aimed at simplifying the underbody leading edge separation, which is challenging to predict consistently, both in experiments²¹ and simulations.²² Both the notch- and squareback configurations were considered, Figs. 2(a) and 2(b). The DrivAer will be described using its standard coordinate system where $x = z = 0$ is located at the front axle and $y = 0$ is at the vehicle centerline.

Racing tires with a nominal size of 210/50R17 were used. They were originally slick, without a tread pattern, but one set was modified to have rain grooves, Fig. 3. Apart from that, they were identical. Since the tires were stiff racing tires, the dynamic deformations by the rotational forces were small. This was demonstrated by Hobeika and Sebben²³ who estimated the rotational forces by large changes in inflation pressure for the same tire sets. The static deformation was replicated for numerical simulations by 3D-scanning the tires while mounted to the vehicle and morphing the CAD. Additionally, plaster castings of the contact patch region were made and scanned to accurately replicate the area that the initial scan could not capture. The tires were mounted to production rims and tested in both an open [see Fig. 2(a)] and in a closed rim configuration, where the latter was achieved by attaching a flat piece of sheet metal to the outer rim surface.

2. Production vehicle

The electric, crossover SUV, Volvo C40 [Fig. 2(c)] was tested in a closed cooling configuration, achieved by taping the front cooling inlets. The tires had a nominal size of 245/45R19 and featured a realistic tread pattern. Contrary to the racing tires used for the DrivAer, these tires will deform under rotational forces. Since the vehicle was attached with fixed struts, constraining the movement of the vehicle body, the radial expansion of the tire compressed the suspension, raising the wheel assembly into the wheelhouse, as described by

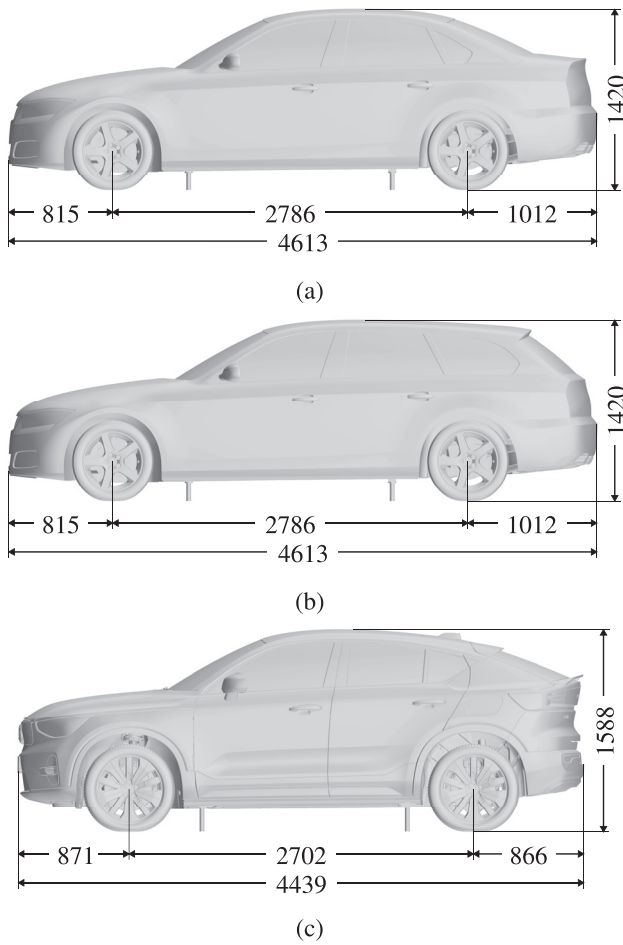


FIG. 2. The three vehicles considered in this work (shown in the same scale) with measurements in millimeters: (a) DrivAer notchback, (b) DrivAer squareback, and (c) Volvo C40.

Landström *et al.*¹¹ Production rims were used [Fig. 2(c)] and a closed rim was obtained by attaching a convex carbon fiber cover.

B. Experimental setup

The experiments were performed in the Volvo Cars Aerodynamic Wind Tunnel (PVT), as described in detail by Sternéus



FIG. 3. Tread patterns considered for the DrivAer: (a) slick and (b) rain grooves.

*et al.*²⁴ PVT has a slotted wall test section and is equipped with a boundary layer control system, Fig. 4. The system consists of a scoop, distributed suction, and a five-belt system with a center belt and four wheel drive units (WDUs). Reynolds number sweeps were performed by increasing the velocity in steps of 20 km/h, starting from 60 km/h. Although the wind tunnel can reach 250 km/h, the boundary layer control system is dimensioned to maintain the flow conditions up to 200 km/h, hence that is the maximum speed considered in this work. For the DrivAer, the maximum velocity was further limited to 160 km/h to avoid damaging the WDU belts due to the high friction produced by the modified racing tires.

For all measurements with rotating wheels, the speed of the WDU belts was the same as the wind speed. Stationary wheel measurements were performed for the C40. For these, all other boundary layer control systems, including the center belt, remained enabled. Previous studies^{13,14} compared moving and stationary ground rather than rotating and stationary wheels, meaning that also the center belt was disabled. However, Walker¹⁰ showed that the state of the center belt has negligible effect on drag reduction with increased speed.

1. Pressure measurements

The DrivAer was equipped with a pressure measurement system, as described by Hubertz *et al.*²¹ Probes were placed along $y = 0$ on both the upper- and underbody, along a constant z cross section at the left-hand side and in the front left wheelhouse, Fig. 5.

For the C40, pressure measurements were conducted in the right-hand side wheelhouses and at the vehicle base. Each wheelhouse was

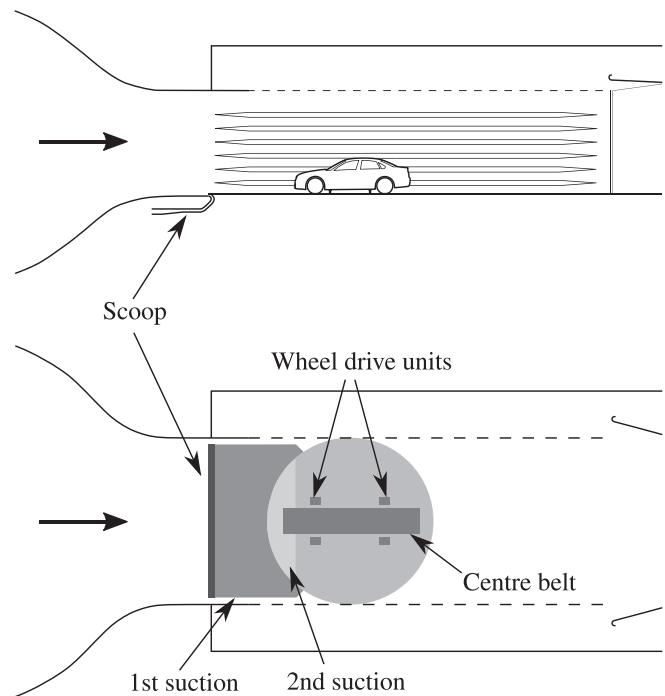


FIG. 4. Boundary layer control system in PVT with the DrivAer drawn to scale. Adapted from Ljungskog *et al.*, *J. Wind Eng. Ind. Aerodyn.* **197**, 104055 (2020). Copyright 2020, with permission from Elsevier.

equipped with nine sensors evenly spaced along the cross section $y = 750$ mm, corresponding to the middle of the tire (Fig. 6). The right-hand side of the base was equipped with 29 sensors with a horizontal and vertical spacing of 150 and 160 mm, respectively. The base drag coefficient, C_{DB} , was calculated by integrating the pressure over the measurement area and multiplying by two to correspond to a full vehicle. This should be valid since both the upper- and underbody are largely symmetric, which was confirmed by symmetric yaw sweeps and flow field measurements (not shown here). First Sensor HCLA0025DB units with a range of ± 2500 Pa were used. The sensors were statically calibrated to within ± 5 Pa.

For a selection of the measurements with the C40, pressures were sampled around the front and rear left-hand side WDUs, Fig. 7. These pressures were measured using a PSI ESP-64HD 64-channel pressure scanner.

All setups used the standard reference pressure in PVT, calculated as $P_\infty = P_{C2} + k_p \Delta P$. Here, P_{C2} is the pressure at the roof of the nozzle contraction, $k_p \approx 0.06$ is a calibration coefficient from the wind tunnel commissioning, and ΔP is the pressure drop over the contraction.

C. Numerical setup

Unsteady numerical simulations were performed for the DrivAer using Star-CCM+. The hybrid delayed detached eddy simulation (DDES) method was used with SST $k-\omega$ in the URANS region near the wall. The numerical setup was similar to that in Ref. 25, where a thorough validation is presented.

The simulations were initialized with a steady-state solution. Next, the domain was flushed using successively finer time steps. The time step at which the solution was averaged was adapted to achieve the same CFL number for all velocities. The averaging time was also adjusted, resulting in 34 flow passages over the vehicle at all velocities. A summary of the time steps and averaging times are shown in Table I.

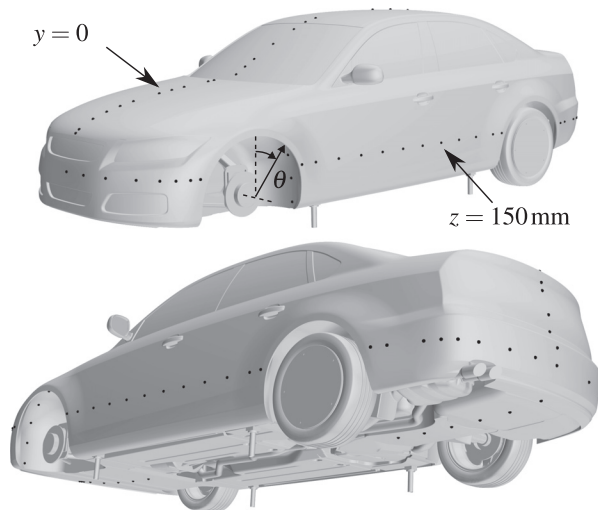


FIG. 5. Pressure probes on the DrivAer. θ is used to describe the probes' positions in the wheelhouse. Note that the front left wheel is hidden.

Since the tires investigated in simulations did not feature any lateral grooves, the entire surface could be accurately modeled as rotating walls. The rims were modeled using sliding mesh.

1. Computational domain

Initial simulations were performed using a detailed model of PVT. However, it was found that the C_D sensitivity to velocity was also replicated in open road conditions. Hence, for more general results,

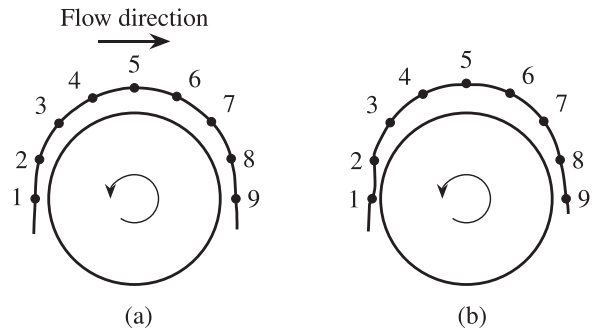


FIG. 6. Placement relative to the wheel and numbering of pressure sensors in the right-hand side front (a) and rear (b) wheelhouses of the C40. The cross section was taken at $y = 750$ mm, approximately at the middle of the wheel.

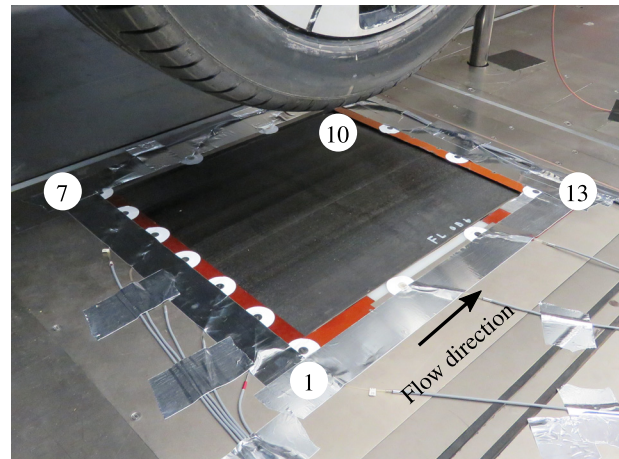


FIG. 7. Pressure spades around the front left WDU. The flow direction and sensor numbering are indicated.

TABLE I. Time step and averaging time for the different velocities.

Velocity, v_∞ (km/h)	Time step, Δt (s)	Averaging time, T (s)
80	4.38×10^{-4}	7.00
100	3.50×10^{-4}	5.60
120	2.92×10^{-4}	4.67
140	2.50×10^{-4}	4.00
160	2.19×10^{-4}	3.50

18 October 2024 08:59:59

the final simulations used an open road sized domain where a generic five-belt system was replicated, Fig. 8. This was preferable over a normal open road setup with fully moving ground since simulations with stationary wheels were also performed. With fully moving ground and stationary wheels, the boundary condition would be unphysical at the tire contact patch. The domain measured $70 \times 40 \times 30 \text{ m}^3$, resulting in a blockage of 0.2%. The vehicle was placed 26 m downstream of the inlet. The five-belt system, consisting of a center belt and four WDUs, was modeled as moving walls with the same velocity as at the inlet. For the cases with stationary wheels, the WDUs were stationary, whereas the center belt remained moving. To obtain a representative boundary layer around the vehicle, the ground upstream of the vehicle, where there is boundary layer suction in the physical wind tunnel, was modeled as a slip wall.

2. Mesh

The same mesh was used for all speeds and was constructed to result in a $y^+ < 1$ at the highest velocity (160 km/h). The mesh consisted of approximately 135×10^6 cells and was hexahedral-dominant with prism layers on all no-slip boundaries. The external vehicle surfaces had ten prism layers that transitioned into 4 mm cells. For the wheels, eight prism cells were used and the surrounding cell size was 2 mm. Figure 9(a) shows the mesh at the centerline of the vehicle along with lines used for evaluating the grid resolution using the two-point correlation of the streamwise velocity, v_x . The lines were placed along the centerline of the base wake ($y = 0$) and downstream of the right-

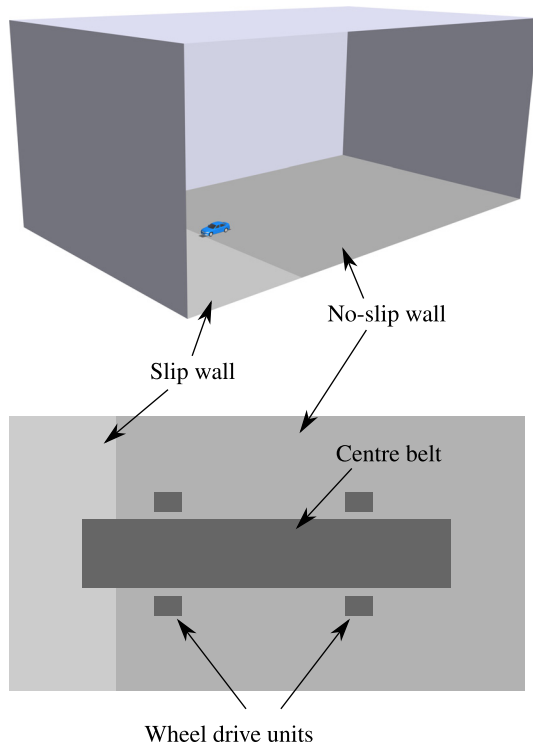


FIG. 8. Computational domain with the vehicle geometry, including a view of the ground simulation setup.

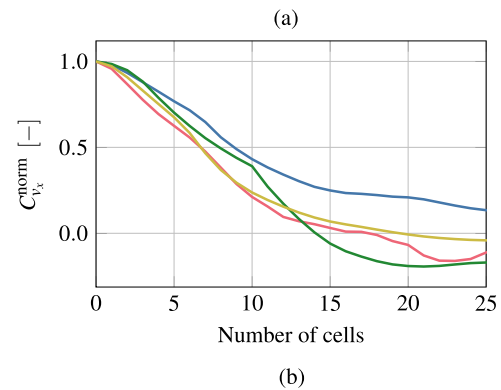
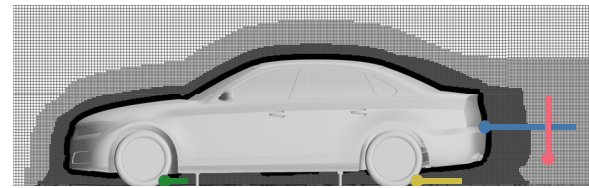


FIG. 9. Mesh and two-point correlation for the DrivAer notchback: (a) Mesh in the plane $y = 0$ and the lines for correlation. The disks mark the start of the lines, which are used as the reference in the calculations. (b) Two-point correlation of the streamwise velocity, v_x , at 160 km/h.

hand side wheels ($y = 750 \text{ mm}$). Davidson²⁶ showed that the two-point correlation gives a better indication of the LES resolution than, for example, the amount of modeled and resolved turbulent kinetic energy. Splitting a variable ζ into its mean and fluctuating part as $\zeta = \bar{\zeta} + \zeta'$, the normalized two-point correlation between two coordinates, \vec{x}_A and \vec{x}_B , is calculated as follows:

$$C_{\zeta}^{\text{norm}}(\vec{x}_A, \vec{x}_B) = \frac{\overline{\zeta'(\vec{x}_A)\zeta'(\vec{x}_B)}}{\zeta'_{\text{RMS}}(\vec{x}_A)\zeta'_{\text{RMS}}(\vec{x}_B)}, \quad (1)$$

$$\zeta'_{\text{RMS}}(\vec{x}) = \overline{\zeta'(\vec{x})^2}^{1/2}.$$

The correlation indicates how well the mesh resolves turbulent structures. For coarse LES, Davidson²⁶ recommended that the largest eddies are resolved by at least eight cells, corresponding to a positive correlation for eight cells. This is fulfilled for all lines, Fig. 9(b).

Additionally, a grid independency study was conducted by coarsening and refining the mesh, resulting in 83×10^6 and 177×10^6 cells, compared to the baseline of 135×10^6 cells. Figure 10 shows the accumulated ΔC_D compared to the baseline. The coarse mesh results in some deviations, most notably around the front wheels. With the fine mesh, the maximum deviation is $0.001 C_D$. Altogether, the baseline mesh is considered sufficient and is used throughout this work.

3. Ventilation moment

Wolf¹⁴ theorized that the drag reduction could be connected to the ventilation moment. Starting from the moment required to rotate the wheels, M_{vent} , the equivalent ventilation force is calculated similarly to Vdovin *et al.*²⁷ as $F_{\text{vent}} = M_{\text{vent}}/r$, where r is the rolling radius.

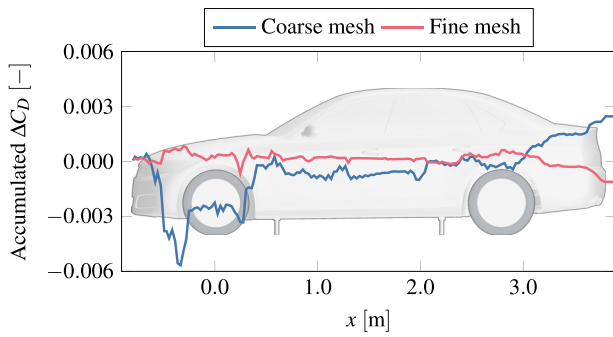


FIG. 10. Accumulated ΔC_D in comparison to the baseline mesh.

Summing the contributions from all four wheels, the C_D equivalent ventilation moment can be expressed as follows:

$$C_{D,vent} = \frac{1}{\frac{1}{2} \rho v_\infty^2 A} \sum_{i=1}^4 \frac{M_{vent,i}}{r_i} \quad (2)$$

D. Uncertainty estimation

For the numerical simulations, the uncertainty of force coefficients due to time averaging of the unsteady signals was estimated. For a signal, ξ , the autocorrelation, $R_{\xi\xi}$, was used to calculate the integral timescale, Λ , as follows:

$$\Lambda = \int_0^\infty R_{\xi\xi}(\tau) d\tau \quad (3)$$

The standard deviation of the time-averaged signal, $\bar{\xi}_T$, was then estimated as follows:

$$\sigma(\bar{\xi}_T) = \sqrt{\frac{2\Lambda}{T}} \sigma(\xi), \quad (4)$$

where T is the averaging time and σ denotes the standard deviation. It was found that Λ changed linearly with velocity. Since the averaging time was scaled with the velocity, Λ/T was approximately constant. The uncertainties presented in this work are 95% confidence intervals, corresponding to $\pm 1.96\sigma(\bar{\xi}_T)$ since the fluctuations were found to be normally distributed.

To estimate the uncertainty of the experimental forces, the standard deviation of repeated measurements within the same test campaign was investigated. These were performed at 100 km/h and a value of $\sigma(C_D) \approx 0.0004$ was found. To understand how the uncertainty scales with the velocity, a large dataset collected for PVT's reference car was utilized. The reference car is regularly tested to check the accuracy and repeatability of the wind tunnel. As part of these regular checks, ten repeated Reynolds sweeps are performed. No significant change in $\sigma(C_D)$ was found for the various velocities. Hence, $\sigma(C_D) = 0.0004$ and the corresponding 95% confidence interval of $\pm 0.0008 C_D$ was used for all velocities.

The uncertainty of the measured pressure coefficients was found to be velocity dependent. Based on a value of $\pm 0.01 C_p$ for 100 km/h, the uncertainties were scaled by $(100 \text{ km/h}/v_\infty)^2$.

As the result of this work will mainly be presented in terms of deltas, the uncertainties are combined as the root-sum-square. The deltas will be calculated toward the measurement at the largest velocity, minimizing the uncertainty. For linear fits, the uncertainties have been propagated following the method labeled standard practice in Hogg *et al.*²⁸

III. RESULTS

A. DrivAer

Figure 11 shows C_D as a function of velocity relative to the value measured at 160 km/h for the DrivAer notchback with rain grooved tires and closed rims. There is a clear, approximately linear, decrease in C_D over the considered velocity range. No velocity sweeps with stationary wheels were carried out during the experimental campaign. Therefore, for completion, the results of James *et al.*¹³ are included. These measurements are also from PVT but with another set of wheels. Nonetheless, the trend is similar for the measurement with ground simulation (GS). For the *No GS* case, both the WDUs and the center belt were disabled, opposite to the rest of this work where the center belt is always enabled. This should however not have a significant impact on the C_D gradient, as shown by Walker.¹⁰ Without ground simulation, C_D is practically constant over the velocity range.

Figure 12 shows the difference in surface pressures between the various velocities with rotating wheels. The reference is the 160 km/h case ($\Delta C_p = C_{p,v_\infty} - C_{p,160\text{km/h}}$). Some differences are observed along the upper body centerline, Fig. 12(a). The transition between the grille and the hood is known to be a sensitive area of the DrivAer.²¹ Since the pressures quickly recover downstream, this likely has no significant global effect. Small variations with limited global impact are also obtained at the end of the hood and at the windscreen ($0.3 \text{ m} \lesssim x \lesssim 1.3 \text{ m}$). A more distinct trend is observed at the rear window. Initially, a higher pressure is obtained for the lower velocities. At around $x = 3.0 \text{ m}$ the behavior reverses, with higher C_p values for the higher speeds. Overall, this contributes to the drag reducing with speed. Although no velocity sweeps were conducted with stationary wheels, the effect is expected to be similar. Measurement at 140 km/h showed no significant change in upper body pressure between rotating and stationary wheels, with a root mean square (RMS) difference of

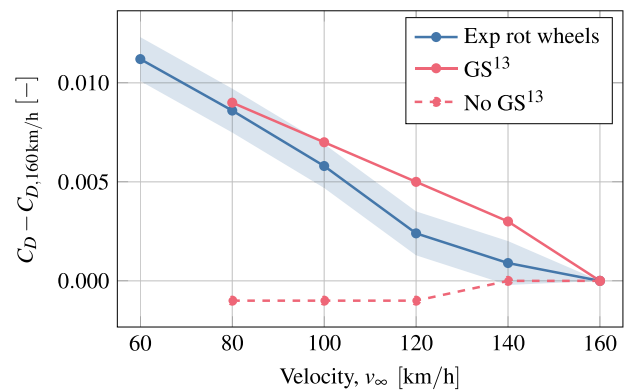


FIG. 11. Drag coefficient relative to the value measured at 160 km/h from experiments with the DrivAer notchback. The blue curve corresponds to results from this test campaign with the filled area marking the 95% uncertainty. GS stands for ground simulation.

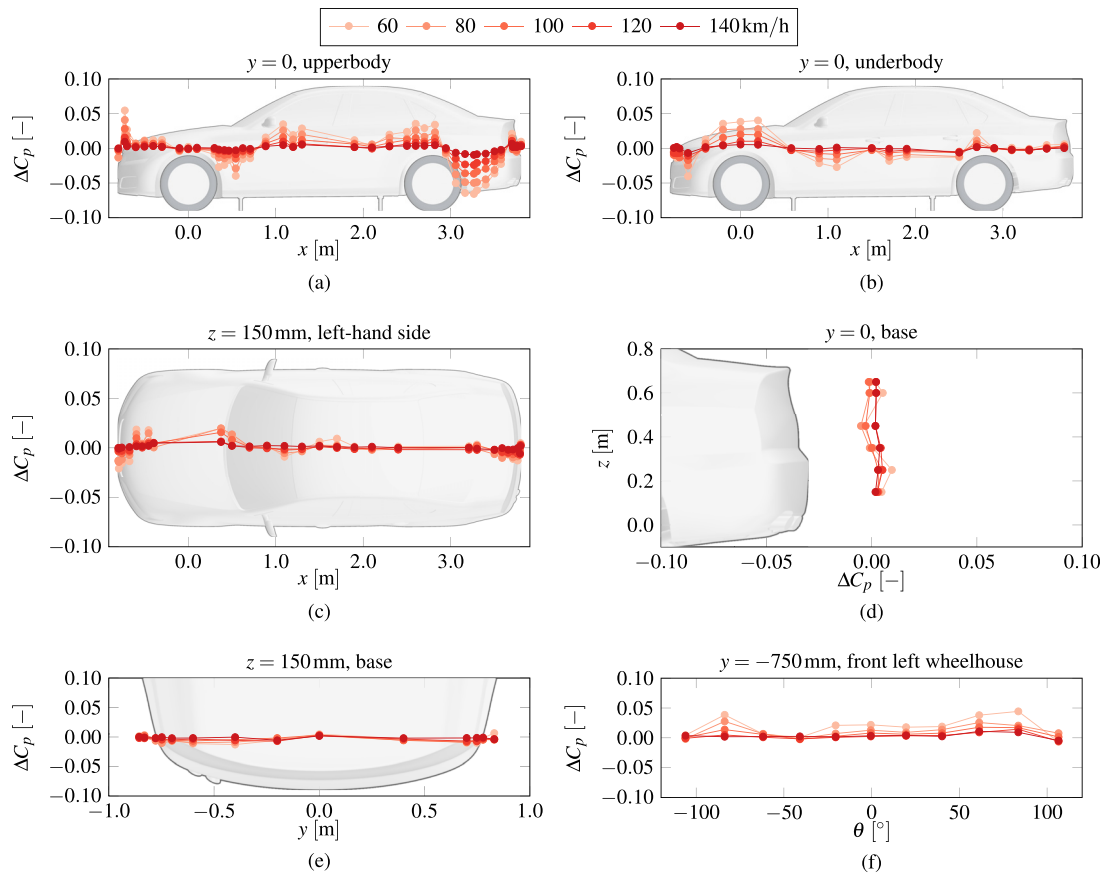


FIG. 12. Variations in C_p at the probes in Fig. 5 compared to the values at 160 km/h. Data from experiments.

0.006 C_p . It is therefore expected that the velocity sensitivity of the rear window pressure is independent of the wheel rotation. Hence, it is not the main explanation for the drag behavior in Fig. 11.

Except for small differences at the underbody leading edge, which is known to be a sensitive area of the DrivAer,²¹ and at the front bumper corner, similar pressures are obtained at the underbody and along the left-hand side at $z = 150$ mm [Figs. 12(b) and 12(c)]. At the base [Figs. 12(d) and 12(e)], the pressures are very similar, meaning that the decreasing C_D is not explained by a change in base pressure.

The pressures in the front left wheelhouse [Fig. 12(f)] are plotted using the polar coordinate θ , as defined in Fig. 5. Some differences are observed at the lower probes ($|\theta| \approx 90^\circ$). The differences themselves do not explain the altered drag since similar variations are obtained at both ends of the wheelhouse, thus canceling their effect. They do, however, imply that the flow around the wheel is altered.

The vehicle was equipped with more pressure probes than those presented here, but apart from the wheelhouse, no clear variations that fully explain the drag reduction are found. It is therefore believed that the main drag-reducing effect does not occur at the vehicle body. Instead, it likely occurs at the wheels, where no pressure measurements were taken.

For further insight, numerical simulations are considered. Figure 13 compares the drag from CFD with rotating and stationary wheels

to the experiments. Overall, the drag reduction is well captured with rotating wheels. The drag is less sensitive with stationary wheels, although a slight velocity dependency is obtained.

The accumulated ΔC_D , Fig. 14, is almost constant over the entire vehicle with stationary wheels. With rotating wheels, the drag increases

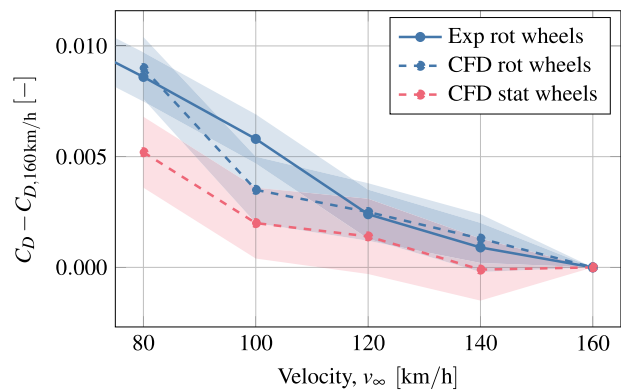


FIG. 13. Difference in C_D compared to the value at 160 km/h. The filled areas mark the 95% uncertainty.

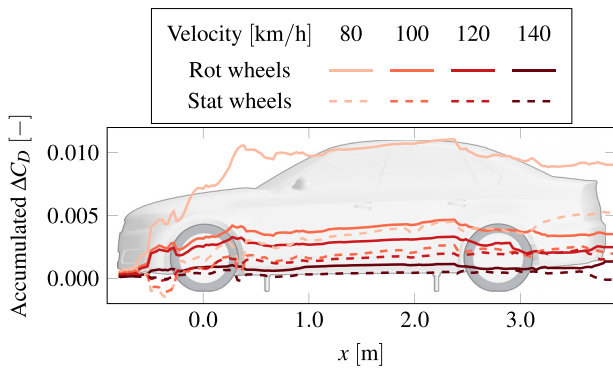


FIG. 14. Accumulated ΔC_D relative to the 160 km/h cases with rotating and stationary wheels. Data from simulations.

over the front wheels for the lower velocities. The differences remain constant until reaching the rear wheels and window, where they reduce slightly. To distinguish between the effects on the window and the rear wheels, the accumulated drag with rotating wheels is split right below the rearview mirrors, Fig. 15. At the rear window (solid lines), the drag difference initially decreases and later switches, resulting in additional drag for the lower velocities. This is consistent with the experimental pressures in Fig. 12(a). Overall, the impact on C_D from the rear window is small. Considering the lower part, $z < 570$ mm, the main variations occur at the front wheels. There is a slight drag decrease at the rear wheels for the lower speeds, reducing the differences between velocities.

Comparing the flow field 40 mm above the ground (Fig. 16) it is clear that the front wheel wake is sensitive to the vehicle velocity for the rotating wheels case. The outer low-energy region widens for the lower velocities, starting from the separation at the tire shoulder, explaining the drag increase. With the larger front wheel wakes, the rear wheels are more shielded from the free-stream flow, explaining the reduction in drag seen in Fig. 15. With stationary wheels, the flow differences between speeds are much smaller.

Figure 17 shows the mean pressure coefficient, C_p , and the corresponding RMS values at the upstream surface of the front left wheel.

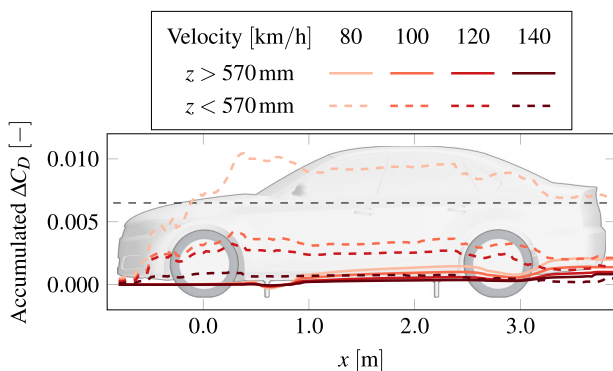


FIG. 15. Accumulated ΔC_D relative to 160 km/h with rotating wheels, split between the tophat and remaining vehicle. The dashed black line marks the split at $z = 570$ mm. Data from simulations.

For the lower velocities, the low-pressure region at the outer contact patch shoulder (bottom right of the figure) shrinks, indicating that the flow is less attached. Comparing the RMS values, a larger region of high fluctuations is observed at the contact patch for the lower velocities, suggesting that the flow separates earlier. For the stationary case, the pressures and fluctuations are similar for all velocities (not shown here).

These results suggest that the main reason for the drag reduction with increasing velocity for the DrivAer is the difference in front wheel separation. The separation's Reynolds number sensitivity differs between rotating and stationary wheels. Additional simulations with stationary front or rear wheels showed a drag reduction only when the front wheels were rotating and were practically independent of the rear wheel state. This is opposite to the measurements by Wolf,¹⁴ suggesting a strong vehicle dependency.

1. Impact of geometrical configuration

Figure 18 shows the drag coefficient delta from experiments with various DrivAer configurations with rotating wheels. All show a drag decrease with increased velocity. Two groups are observed. The first, consisting of all notchback configurations except rain grooved tires with open rims, has a drag decrease of $0.011 - 0.012 C_D$ between 60 and 160 km/h. The second group, containing all squareback configurations and the remaining notchback variant, has a reduction of $0.006 - 0.008 C_D$ over the same velocity range. The variants can be characterized by the slope, k , of a linear fit $C_D(v_\infty) = kv_\infty + m$, Fig. 19. As seen, k is similar for all notchback configurations except for rain grooved tires on open rims, which has a value comparable to the squareback configurations.

The difference between the notch- and squareback is believed to be caused by the notchback's rear window separation. Figure 20 shows the accumulated ΔC_D for the two rear-ends with rain grooved tires and closed rims. As illustrated by the 80 km/h line, the drag increase is identical until the start of the notchback's rear window. As discussed in connection to Figs. 12(a) and 15, the Reynolds sensitivity of the rear window has a small contribution to the drag decrease. This is again illustrated by ΔC_p , Fig. 21. With the well-defined separation on the squareback, no considerable difference in base pressure is obtained.

Comparing closed and open rims in Fig. 19, there are no significant differences in the C_D gradient apart from the notchback with rain grooved tires, where the reduction is less for the open rim. As the ventilation moment should be larger with the open rim, these results do not follow the hypothesis by Wolf.¹⁴ The ventilation moment was not measured during the experimental campaign. Numerically, the C_D equivalent ventilation moment was found to be higher for the open than for the closed rim, 0.009 compared to 0.007 at 160 km/h (corresponding to approximately 3% of C_D), which is in line with previous studies.^{9,23,27} Similar to the drag, the ventilation moment decreases with increased velocity, Fig. 22. The reduction is much smaller than for C_D .

Since a rim dependency is only observed with the rain grooved tire, it is believed to be an interference effect between the rain grooves and rim design. The dependency is seen for 60 and 80 km/h in Fig. 18 (blue curves). Between 100 and 160 km/h, all notchback configurations are similar. The same trend is obtained in simulations (Fig. 23), where differences occur at the front wheel, most clearly at 80 km/h. Comparing $\Delta C_{p_{tot}}$ at the front left wheel, there is a larger change in the

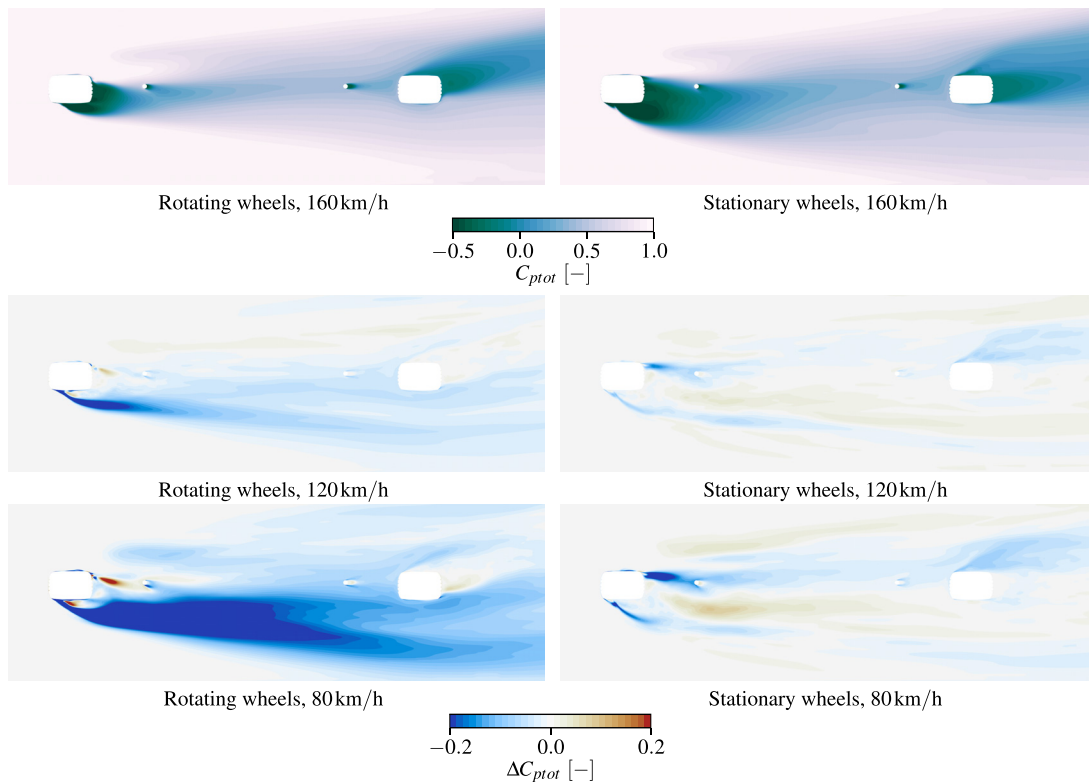


FIG. 16. Total pressure coefficient, C_{ptot} , at 160 km/h and the corresponding ΔC_{ptot} 40 mm above the ground at the left-hand side. Data from simulations.

contact patch separation with the closed rim, Fig. 24. For both rims, the differences start at the leading edge of the contact patch, spreading upward and downstream. With the open rim, the region of negative ΔC_{ptot} remains below the rim edge. An explanation for this could be that, with the open rim, the rotation of spokes dominates the flow field, mitigating part of the Reynolds sensitive separation at the tire

shoulder. With the closed rim, the flow is instead mainly characterized by the tire. No rim dependency was found for the slick tire in the wind tunnel measurements. The reason for this is not entirely understood since the simulations did not fully capture the experimental trend. The simulations did, however, indicate that it could be due to the separation at the tire mid-height.

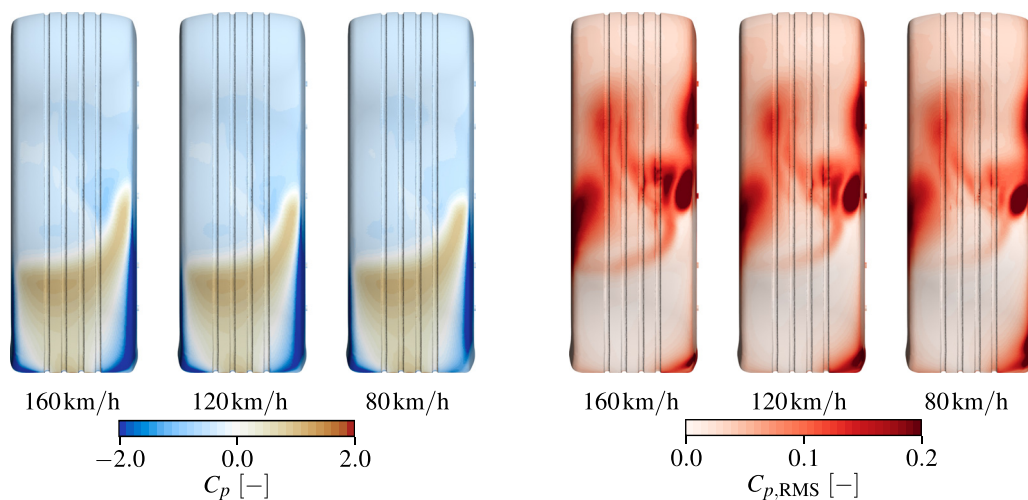


FIG. 17. Mean pressure coefficient and the corresponding root mean square values at the front left tire for rotating wheels. Seen from the front. Data from simulations.

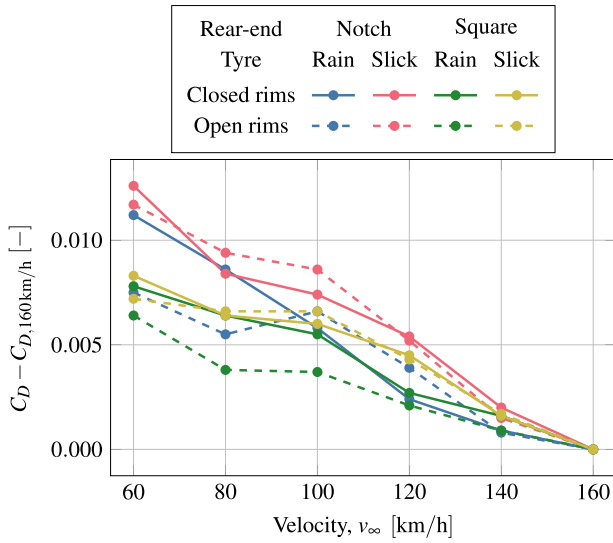


FIG. 18. Drag coefficient relative to the value measured at 160 km/h for the various DrivAer configurations. The uncertainty of $\pm 0.0008 C_D$ has been omitted for readability. Data from experiments.

In summary, it is concluded that the main explanation for the C_D decrease at higher velocities for the DrivAer likely is a reduction in the size of the front wheel outer contact patch separation. The degree of drag reduction should therefore be strongly dependent on the tire shoulder geometry. This was reinforced by performing additional simulations with a more rounded tire shoulder, which significantly reduced the drag gradient, Fig. 25.

B. Production vehicle

To investigate the generality of the DrivAer results, an experimental test campaign was performed with a production vehicle. The vehicle was the Volvo C40 crossover SUV, which has similar

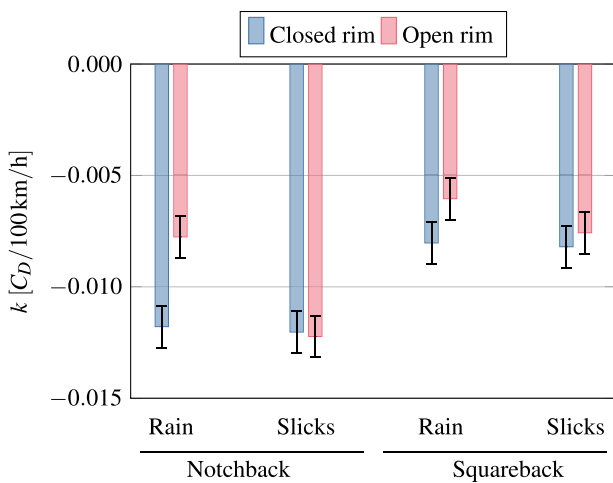


FIG. 19. Linear slope, k , for the DrivAer configurations presented in Fig. 18. Data from experiments.

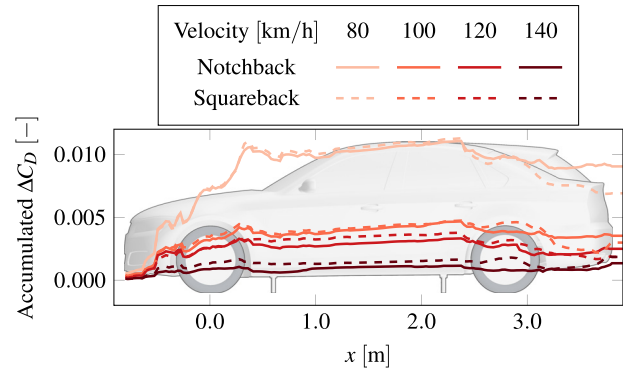


FIG. 20. Accumulated ΔC_D relative to 160 km/h for the two rear-ends with rain grooved tires and closed rims. Data from simulations.

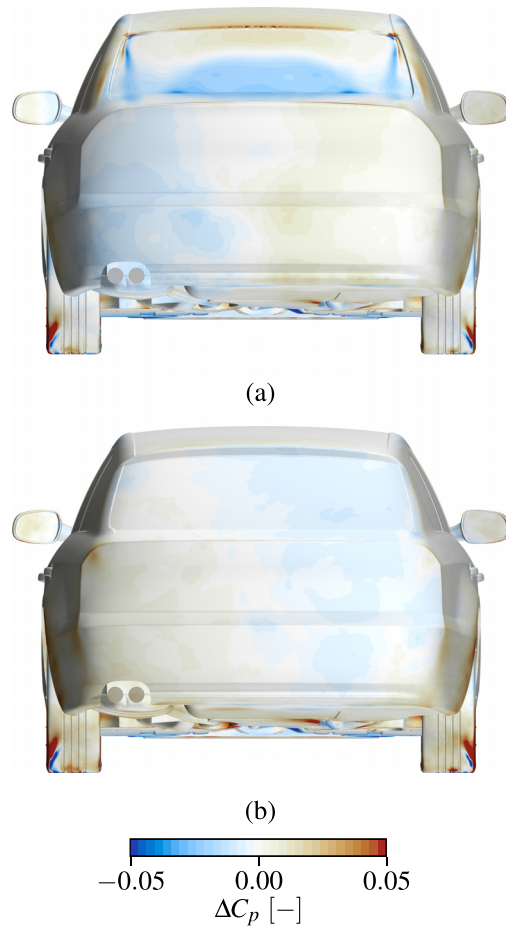


FIG. 21. Difference in C_p between 80 and 160 km/h for the two rear-ends: (a) notchback and (b) squareback. The configuration is the rain grooved tires with closed rims. Data from simulations.

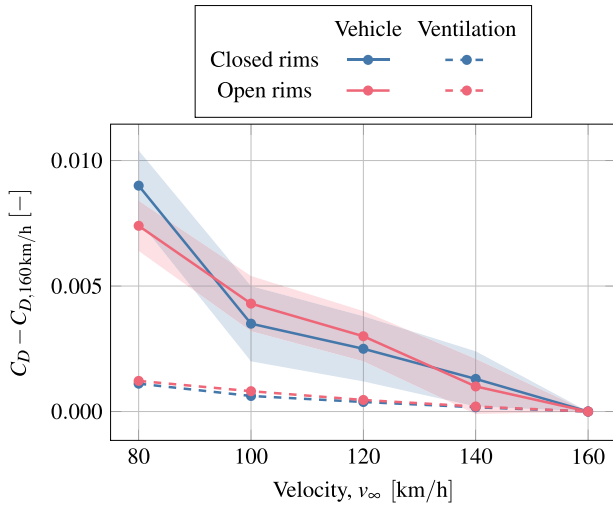


FIG. 22. Difference in C_D and C_D equivalent ventilation moment compared to the values at 160 km/h for closed and open rims with the rain grooved tire. The filled areas mark the 95% uncertainty. The uncertainty of the ventilation moments is on the order of $10^{-5} C_{D,vent}$ and is therefore omitted. Data from simulations.

dimensions as the vehicle investigated by Wolf.¹⁴ Figure 26 shows the change in drag for closed and open rims with different wheel rotational states. The production model could be tested at velocities up to 200 km/h, hence the deltas are calculated toward this velocity. Both closed and open rims result in a drag decrease in $0.003\text{--}0.004 C_D/100$ km/h with all wheels rotating, which is significantly less than for the DrivAer or the vehicle investigated in Ref. 14. With stationary wheels, there is almost no velocity dependency for either of the rims. Opposite to the DrivAer, but similar to Ref. 14, the drag reduction only occurs when the rear wheels are rotating (*All rot* and *Rear rot*). Depending on the front wheel state, the degree of reduction is altered. With the closed rim, the steepest decline is measured with only the rear wheels rotating (*Rear rot*). With the open rim, *Rear rot* gives a slope in between all wheels rotating and all wheels stationary. This dependency is likely explained by how the front wheel wakes shield the rear wheels. As shown for the DrivAer in Fig. 16, the front wheel rotation greatly

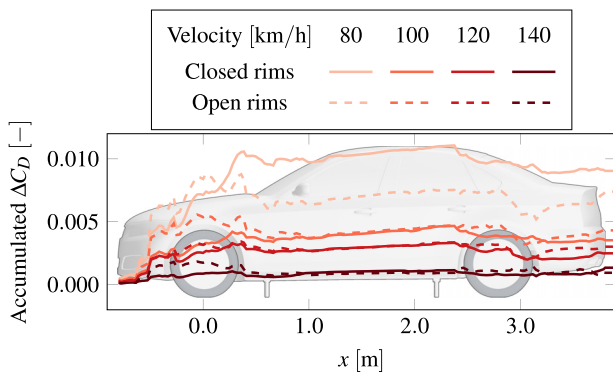


FIG. 23. Accumulated ΔC_D toward the 160 km/h cases comparing closed and open rims with the rain grooved tire. Data from simulations.

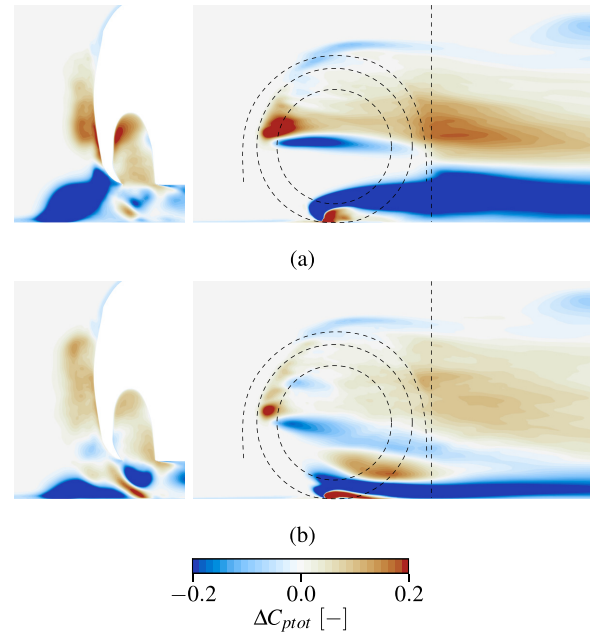


FIG. 24. ΔC_{ptot} between 80 and 160 km/h in an x -normal plane 400 mm downstream of the wheel axle (left) and a y -normal plane 25 mm outside the tire bulge (right) for the rain grooved tire on the closed (a) and open (b) rims. The dashed lines mark the outline of the tire, rim, and wheelhouse as well as the location of the x -normal plane. Data from simulations.

affects the size and direction of the wakes. As shown in Ref. 29, for the same production vehicle, the wake size and direction are also altered between closed and open rims. The interaction between the rim design and wheel rotation changes the flow upstream of the rear wheel, explaining the responses to front wheel rotation in Fig. 26.

Using base pressure measurements, the base drag was calculated. Figure 27 shows the difference in base drag coefficient, C_{DB} , relative to 200 km/h for the closed rim. Considering that the uncertainty is larger for the lower velocities, there is no significant change in base drag with speed for any of the wheel rotational states.

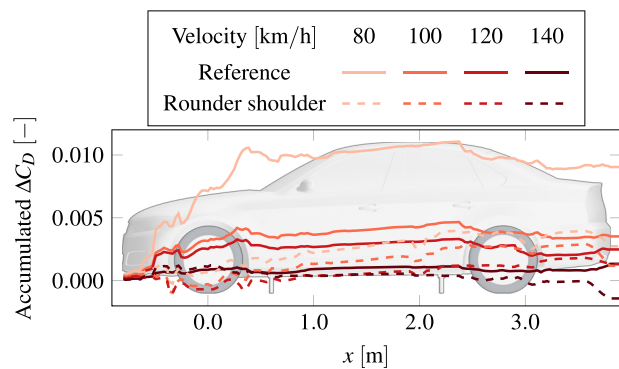


FIG. 25. Accumulated ΔC_D relative to 160 km/h for two tire shoulder geometries with closed rims. Data from simulations.

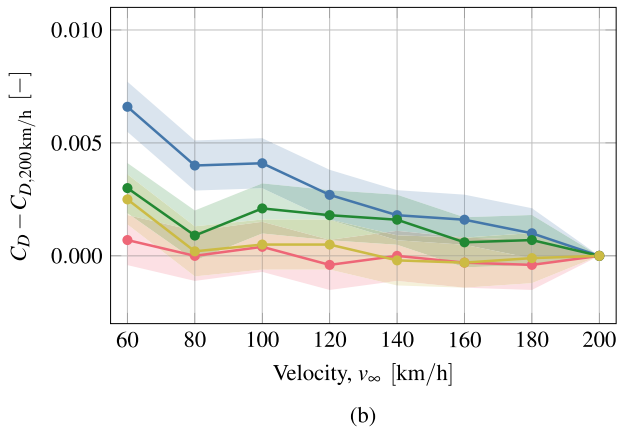
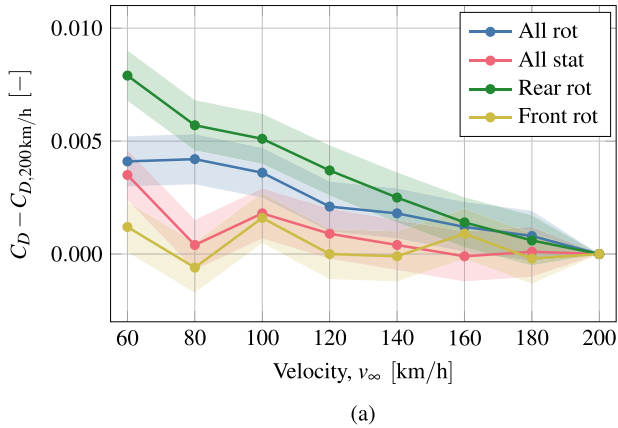


FIG. 26. ΔC_D compared to 200 km/h for the production vehicle with different rims and wheel rotational states. Data from experiments. (a) Closed rim and (b) open rim.

Pressure measurements were also taken in the front and rear wheelhouses. These pressures alone do not give a complete explanation for the drag behavior in Fig. 26, since the main variations are believed to occur on the exposed parts of the tire shoulders, as was observed for

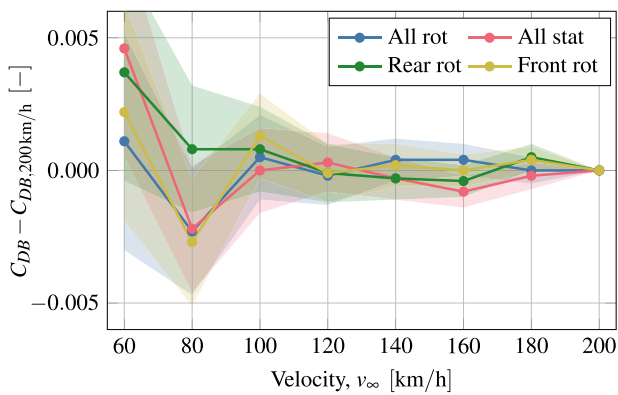
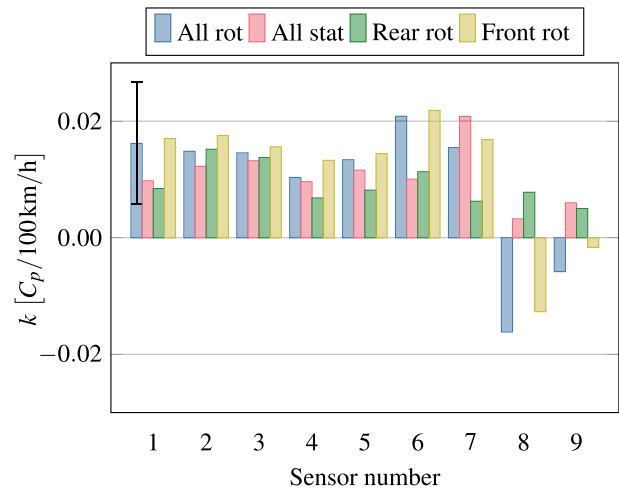
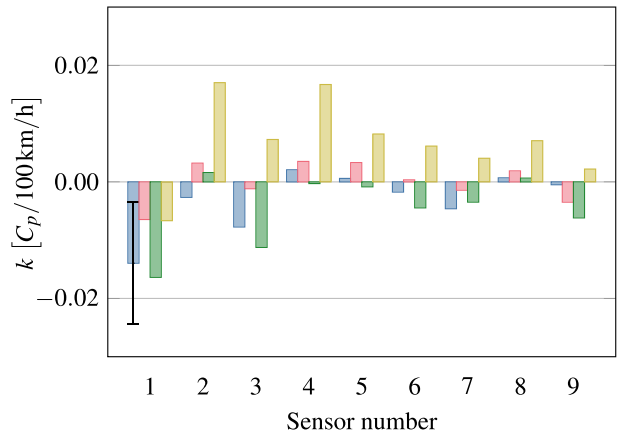


FIG. 27. Difference in base drag coefficient, C_{DB} , for various wheel rotational states with the closed rim. Data from experiments.

the DrivAer. They are, however, useful for studying where changes occur with the different wheel rotational states. Figure 28 shows the slope, k , of the linear fit $C_p(v_\infty) = kv_\infty + m$ for each probe with the four wheel rotational states. A positive value indicates that the pressure increases for higher velocities. Although the slopes are small compared to the uncertainty, some general trends can be observed. At the front wheel [Fig. 28(a)], the velocity sensitivity is mainly affected by the front wheels' rotational state. With rotating front wheels (*All rot* and *Front rot*), C_p increases with speed in the front and top of the wheelhouse (sensors 1–7) and reduces with speed further rearward (sensors 8 and 9). Since the pressures at sensors 1, 2, 8, and 9 are most influential for drag, this will contribute to drag reducing with speed. With stationary front wheels (*All stat* and *Rear rot*), a positive k is obtained for all sensors, meaning that the flow field is altered with speed, but that the net drag effect on the wheelhouse will be close to zero.



(a) Front wheel



(b) Rear wheel

FIG. 28. Linear slope of wheelhouse pressures when varying the velocity for different wheel rotational states with the closed rim. The probe numbering is according to Fig. 6. The uncertainty is the same for all bars. For readability, it is only shown for the first bar. Data from experiments. (a) Front wheel and (b) rear wheel.

A more complex flow is obtained at the rear wheel since its inflow is dependent on the front wheel rotational state, Fig. 28(b). If the rear wheels are rotating, the pressure trends are however independent of the front wheel rotational state (*All rot* and *Rear rot* are similar). A negative k is obtained for sensor 1, potentially mitigating some of the drag reduction in the front wheelhouse, similar to the observations for the DrivAer in Fig. 15. The sensitivity is low for the remaining sensors. A different trend is obtained with stationary rear wheels (*All stat* and *Front rot*). With all wheels stationary, the pressures at all sensors are insensitive. Combined with the drag canceling effect in the front wheelhouse, the constant C_D [Fig. 26(a)] is motivated. With rotating front and stationary rear wheels (*Front rot*), there is a clear velocity dependence. This in itself is not enough to explain why the drag is unaffected by changes in velocity, but it highlights the complex interaction between the front wheel wake and the rear wheel.

Figure 29 compares the pressures around the left-hand side WDUs, measured using the setup in Fig. 7, with the slope k for a linear fit plotted at the right axis. These measurements were only performed with all wheels rotating. Note that the pressure differences are greater than in the wheelhouse, with k one order of magnitude larger. At the front wheel [Fig. 29(a)], the sensors right upstream of the tire (4–6) are insensitive to changing velocity. Closer to the upstream tire shoulders (1–3, 7, 8, and 15), a clearer dependency is observed. Increasing the speed, the pressure drops at the upstream outside corner and decreases at the inside of the wheel. To connect these changes to variations in the flow structures, the pressure distribution on and around the WDUs from CFD at 100 km/h, as presented and validated in Ref. 30, is used as a reference, Fig. 30. At the front wheel, increased speed leads to lower pressure at sensor 15, suggesting that the low-pressure zone at the outer shoulder is enlarged. This can be associated with a more

attached flow at the tire shoulder, similar to the observations with the DrivAer. At the inside of the tire (sensors 7–10), the pressure increases with speed. These effects were observed in Ref. 30 when the flow was more attached at the outside, shifting the balance of flow between the inner and outer sides of the tire.

The pressure distribution is more uniform at the rear wheel, Fig. 29(b). Generally, the pressure increases slightly with speed. This is thought to be caused by differences in the shielding provided by the front wheel wake, which is dependent on the shoulder separation.

C. Final remarks and comparison to previous studies

The results with the DrivAer show that dynamic tire deformation is not necessary to observe the drag-reducing effect with increasing speed. This differs from the results for a squareback DrivAer with rigid alloy wheels presented by Reiß.¹⁵ One reason for this could be that the flow is sensitive to the tire shoulder geometry at the contact patch, as shown in this work. With rigid wheels, the static deformation is neglected, creating an unrealistic contact patch. Even though dynamic deformation is not required to obtain the drag reduction, it is believed to increase the degree of reduction since the tire contracts axially with speed, resulting in a narrower tire that is expected to have lower drag.

Using base pressure measurements, it was shown that the drag reduction with increased speed could not be attributed to lower base drag, as theorized by Wolf.¹⁴ Rear wheel rotation was required to obtain the drag-drop for the vehicle used in Ref. 14. This was confirmed for the production vehicle but not for the DrivAer. The wheelhouse pressure measurements indicated that there is a complex interaction between the front wheel wakes and rear wheels and that the interaction differs depending on the wheels' rotational state. It is

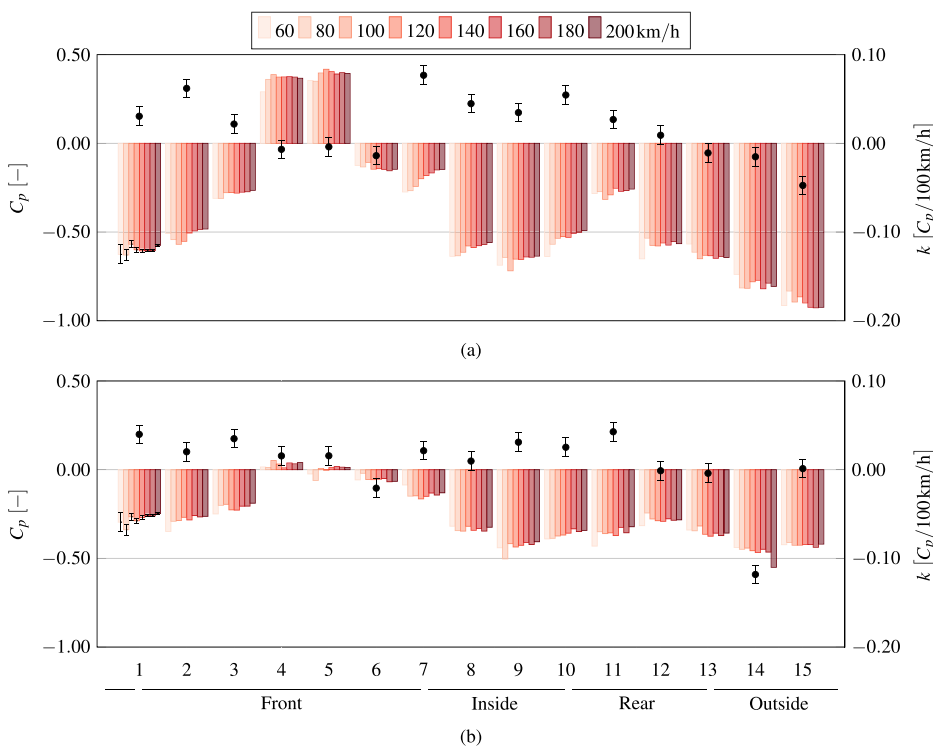


FIG. 29. Pressure coefficient and corresponding linear slope, k , around the left-hand side front (a) and rear (b) WDUs with the closed rim configuration. The sensor numbering is according to Fig. 7. The uncertainty of C_p is the same for all probes but is only shown for probe 1 for readability. Data from experiments.

18 October 2024 08:59:59

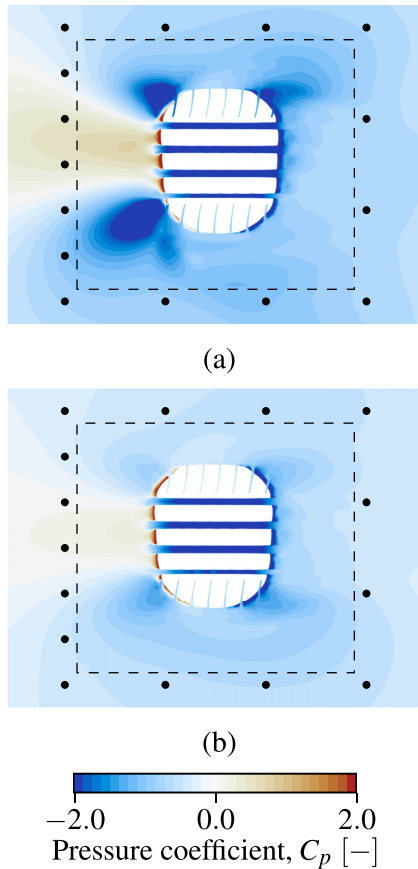


FIG. 30. Pressure coefficient on the ground around the front (a) and rear (b) left-hand side wheels from numerical simulations with the closed rim at 100 km/h. The dashed line marks the outline of the WDU and the dots mark the location of the experimental pressure measurements.

reasonable to believe that this interaction is vehicle-dependent. Some of these variations could be due to the simplifications of the DrivAer, such as a lack of front wheel deflectors, altering the flow around the wheels.

Varying the rim design, Wolf¹⁴ found that the rate of drag reduction increased for larger diameter rims, which was connected to increased rim opening area and potentially larger ventilation moment. In this study, no significant impact of the rim opening area was observed for either of the vehicles. In Ref. 14, the tire size was adjusted for the different rims such that the wheel diameter was approximately constant, meaning that tires with lower sidewall profiles were used for the larger rims. This could explain the steeper drop in drag with bigger rims since low-profile tires typically have a smaller shoulder radius. The dependency on the shoulder radius is shown for the DrivAer in Fig. 25. As part of the experimental campaign with the production vehicle, tires with different tread and sidewall profiles were evaluated. Figure 31 compares the minimum shoulder radius of each tire to its corresponding slope, k , of a linear fit $C_D(v_\infty) = kv_\infty + m$. For tires with a sharper shoulder (smaller radius), the drag sensitivity to velocity is typically larger, indicating that it is an important parameter.

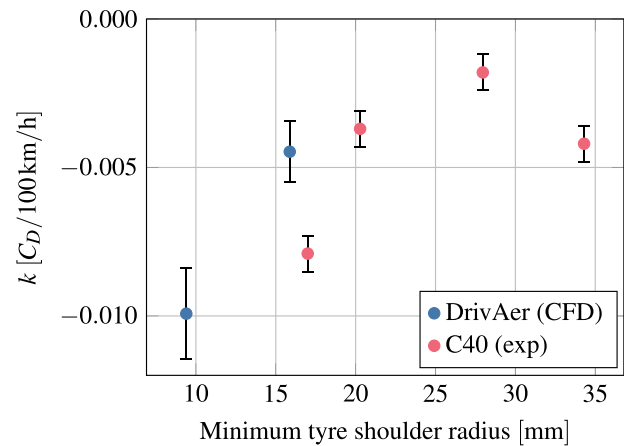


FIG. 31. Linear slope, k , in relation to the minimum radius of the tire shoulder. The data for the DrivAer are from the CFD simulations in Fig. 25. For the production vehicle, three additional tires evaluated during the same test campaign are included.

However, as indicated by the k -value for the largest radius, it is not the sole explanation for the sensitivity.

IV. CONCLUSIONS

In this study, the drag sensitivity to the Reynolds number was investigated for the DrivAer and a production vehicle. With rotating wheels, the drag coefficient decreased with increasing speed, whereas it was practically constant with stationary wheels. From experimental pressure measurements with the DrivAer, it was concluded that the drag reduction could not be explained by changes on the vehicle body. With the help of CFD simulations, it was established that the separations at the front wheels' outer tire shoulders have a great impact on the drag sensitivity to velocity and that the dynamic deformation of the tire is not required to create this effect. The drag reduction was only obtained when the front wheels rotated and was almost independent of the rear wheels' rotational state.

Comparing different configurations, it was shown that the separation over the DrivAer notchback rear window contributed slightly to the drag reduction, resulting in a steeper decrease than with the squareback. No difference in drag reduction was measured between closed and open rims or between rain grooved and slick tires, except when combining the open rim and the rain grooved tire.

The velocity dependency was smaller with the production vehicle. Using different wheel rotational states, it was shown that rear wheel rotation was required to obtain the drag reduction, opposite to the DrivAer. Comparing the wheelhouse pressures highlighted the complex interaction between the front wheel wakes and the rear wheels, where the front wheel rotational state altered the velocity sensitivity of the rear wheelhouse pressures. Using pressure measurements on the wind tunnel floor and comparing them to a reference simulation, it was found that the separation at the front tires' outer shoulder likely contributed to the drag reduction, similar to the DrivAer. It was shown that a sharper tire shoulder typically resulted in a steeper drag reduction.

This work reaffirms that the drag coefficient is Reynolds number dependent within the range relevant for vehicle aerodynamics when

testing with rotating wheels. The main reason is believed to be a Reynolds number sensitive separation at the outer tire shoulder. The results highlight the need to be aware of this sensitivity since it can affect both absolute drag values and drag deltas between configurations.

ACKNOWLEDGMENTS

The authors would like to thank Ford of Europe, particularly Dr. Burkhard Hupertz and Manfred Lentzen, for making the DrivAer available and sharing their expertise on the model. The prototype tires used for the Volvo C40 were supplied by Pirelli Tyre SpA. In particular, Dr. Luca Camosi (Pirelli) and Ph.D. candidate Fabio Semeraro (Politecnico di Milano) are acknowledged for their contributions to the project. The authors would also like to thank Fabio Semeraro for sharing the measurements with an isolated wheel in Fig. 1. The numerical simulations were enabled by resources provided by the National Academic Infrastructure for Supercomputing in Sweden (NAISS) partially funded by the Swedish Research Council through Grant Agreement No. 2022-06725. This work is funded by the Swedish Energy Agency (Grant No. P49114-1).

AUTHOR DECLARATIONS

Conflict of Interest

The authors have no conflicts to disclose.

Author Contributions

Erik Josefsson: Conceptualization (equal); Data curation (equal); Formal analysis (equal); Investigation (equal); Methodology (equal); Software (equal); Validation (equal); Visualization (equal); Writing – original draft (equal). **Magnus Urquhart:** Conceptualization (supporting); Funding acquisition (supporting); Methodology (supporting); Project administration (lead); Resources (equal); Supervision (equal); Writing – review & editing (supporting). **Simone Sebben:** Conceptualization (equal); Funding acquisition (equal); Methodology (equal); Resources (equal); Supervision (equal); Writing – review & editing (equal).

DATA AVAILABILITY

The data that support the findings of this study are available from the corresponding author upon reasonable request.

REFERENCES

- T. C. Schuetz, *Aerodynamics of Road Vehicles*, 5th ed. (SAE International, Warrendale, PA, 2015).
- A. Cogotti, “Aerodynamic characteristics of car wheels,” *Int. J. Veh. Des.* **173**–196 (1983).
- G. Wickern, K. Zwicker, and M. Pfadenhauer, “Rotating wheels—Their impact on wind tunnel test techniques and on vehicle drag results,” *SAE Trans.* **106**, 254–270 (1997).
- E. Mercker, N. Breuer, H. Berneburg, and H. Emmelmann, “On the aerodynamic interference due to the rolling wheels of passenger cars,” *SAE Trans.* **100**, 460–476 (1991).
- P. Elofsson and M. Bannister, “Drag reduction mechanisms due to moving ground and wheel rotation in passenger cars,” *SAE Trans.* **111**, 591–604 (2002).
- A. Wäschle, “The influence of rotating wheels on vehicle aerodynamics—Numerical and experimental investigations,” SAE Technical Paper 2007-01-0107, 2007. 10.4271/2007-01-0107.
- C. Landström, L. Löfdahl, and T. Walker, “Detailed flow studies in close proximity of rotating wheels on a passenger car,” *SAE Int. J. Passeng. Cars - Mech. Syst.* **2**, 861–874 (2009).
- Y. Wang, C. Sicot, J. Borée, and M. Grandemange, “Experimental study of wheel-vehicle aerodynamic interactions,” *J. Wind Eng. Ind. Aerodyn.* **198**, 104062 (2020).
- W. Mayer and J. Wiedemann, “The influence of rotating wheels on total road load,” SAE Technical Paper 2007-01-1047, 2007. 10.4271/2007-01-1047.
- T. Walker, “Effects of wheel rotation on aerodynamic drag in the Volvo moving belt wind tunnel,” 2007.
- C. Landström, L. Josefsson, T. Walker, and L. Löfdahl, “Aerodynamic effects of different tire models on a sedan type passenger car,” *SAE Int. J. Passeng. Cars - Mech. Syst.* **5**, 136–151 (2012).
- A. Vdovin, L. Löfdahl, S. Sebben, and T. Walker, “Investigation of vehicle ride height and wheel position influence on the aerodynamic forces of ground vehicles,” in *The International Vehicle Aerodynamics Conference* (Woodhead Publishing, Loughborough, 2014), pp. 81–90.
- T. James, L. Krueger, M. Lentzen, S. Woodiga, K. Chalupa, B. Hupertz, and N. Lewington, “Development and initial testing of a full-scale DrivAer generic realistic wind tunnel correlation and calibration model,” *SAE Int. J. Passeng. Cars - Mech. Syst.* **11**, 353–367 (2018).
- T. Wolf, “Effect of wheel rotational speed on the drag of a sport utility vehicle coupé and the aerodynamic evaluation of wheelsets,” SAE Technical Paper 2022-01-5041, 2022. 10.4271/2022-01-5041.
- J. Reiß, “Tire effects on vehicle aerodynamics,” Ph.D. thesis, Technische Universität München, 2023.
- F. Wittmeier, *Ein Beitrag Zur Aerodynamischen Optimierung Von Pkw Reifen*, Wissenschaftliche Reihe Fahrzeugtechnik Universität Stuttgart (Springer Vieweg, Wiesbaden, 2014).
- P. Leśniewicz, M. Kulak, and M. Karczewski, “Vehicle wheel drag coefficient in relation to travelling velocity—CFD analysis,” *J. Phys.* **760**, 012014 (2016).
- A. Morelli, “Aerodynamic effects on an automobile wheel,” *ATA Rev.* **22**(6), 281–288 (1969).
- F. F. Semeraro, “Reynolds sweep with isolated rotating wheel,” 2024.
- A. I. Heft, T. Indinger, and N. A. Adams, “Introduction of a new realistic generic car model for aerodynamic investigations,” SAE Technical Paper 2012-01-0168, 2012. 10.4271/2012-01-0168.
- B. Hupertz, K. Chalupa, L. Krueger, K. Howard, H.-D. Glueck, N. Lewington, J.-H. Chang, and Y.-s. Shin, “On the aerodynamics of the notchback open cooling DrivAer: A detailed investigation of wind tunnel data for improved correlation and reference,” SAE Technical Paper 2021-01-0958, 2021. 10.4271/2021-01-0958.
- N. Ashton, V. Skaperdas, O. Sinclair, and W. Van Noordt, in *First Automotive CFD Prediction Workshop, Cross-Plotting—Case2a/b* (Oxford, 2019).
- T. Hobeika and S. Sebben, “Tyre pattern features and their effects on passenger vehicle drag,” *SAE Int. J. Passeng. Cars - Mech. Syst.* **11**, 401–413 (2018).
- J. Sternéus, T. Walker, and T. Bender, “Upgrade of the Volvo cars aerodynamic wind tunnel,” SAE Technical Paper 2007-01-1043, 2007. 10.4271/2007-01-1043.
- E. Josefsson, T. Hobeika, and S. Sebben, “Evaluation of wind tunnel interference on numerical prediction of wheel aerodynamics,” *J. Wind Eng. Ind. Aerodyn.* **224**, 104945 (2022).
- L. Davidson, “Large eddy simulations: How to evaluate resolution,” *Int. J. Heat Fluid Flow* **30**, 1016–1025 (2009).
- A. Vdovin, L. Löfdahl, and S. Sebben, “Investigation of wheel aerodynamic resistance of passenger cars,” *SAE Int. J. Passeng. Cars - Mech. Syst.* **7**, 639–645 (2014).
- D. W. Hogg, J. Bovy, and D. Lang, “Data analysis recipes: Fitting a model to data,” [arXiv:1008.4686](https://arxiv.org/abs/1008.4686) (2010).
- E. Josefsson, S. Sebben, and M. Urquhart, “Characterisation of the flow around passenger vehicle wheels with varying tyre profiles,” *Int. J. Heat Fluid Flow* **103**, 109191 (2023).
- E. Josefsson, M. Urquhart, and S. Sebben, “Wheel drive unit lift corrections in automotive wind tunnels,” SAE Technical Paper 2024-01-2544, 2024. 10.4271/2024-01-2544.